J. Fluid Mech. (2011), *vol.* 677, *pp.* 154–178. © Cambridge University Press 2011
doi:10.1017/jfm.2011.74

Columnar eddy formation in freely decaying homogeneous rotating turbulence

K. YOSHIMATSU†, M. MIDORIKAWA AND Y. KANEDA

Department of Computational Science and Engineering, Nagoya University, Nagoya 464-8603, Japan

(Received 19 September 2009; revised 27 July 2010; accepted 9 February 2011; first published online 18 April 2011)

The roles of the Coriolis force and the convection associated with the fluid motion in the formation of columnar eddies in freely decaying homogeneous rotating turbulence at a moderate Rossby number are studied by direct numerical simulation of the Navier–Stokes equations in a periodic box. The simulated field is compared with a series of artificial fields generated by switching off the nonlinear and viscous terms in the Navier–Stokes equation at given instants. The comparison shows that, without the nonlinear convection effect, the Coriolis force cannot sustain the substantial growth in the direction parallel to the rotational axis of the length scale defined on the basis of the two-point correlation of the square of the vorticity, i.e. cannot sustain the formation of the columnar eddies. The length scale characterizes well the intuitive impression from visualization of flow obeying the dynamics with or without the nonlinear effect. It is shown that the lack of substantial growth is insensitive to the scale of the eddies, the box size and viscosity, at least in the case studied here.

Key words: homogeneous turbulence, rotating turbulence

1. Introduction

Rotating turbulent flows subject to the Coriolis force play important roles in astrophysics, geophysics and engineering. Columnar structures elongated in the direction parallel to the rotation axis are often observed in such flows (e.g. Hopfinger, Browand & Gagne 1982; Bartello, Métais & Lesieur 1994). It is then natural to ask: 'What causes the formation of the structures?' or 'What is responsible for the formation?' There have been studies to answer the questions. But the issue seems not to be yet settled.

One might think that the formation of the columnar structures can be explained by the Taylor–Proudman theorem. According to this theorem, the flow field subject to strong enough Coriolis force must be two-dimensional. However, the theorem presumes that the time dependence of the flow field is negligible, while it is not the case in the turbulence. The Taylor–Proudman theorem has been recognized to be insufficient for the understanding of the formation of the columnar structures in many previous studies including Cambon *et al.* (1994), Cambon, Mansour & Godeferd (1997), Yeung & Zhou (1998), Cambon & Scott (1999), Cambon, Rubinstein & Godeferd (2004), Bellet *et al.* (2006).

† Email address for correspondence: yosimatu@fluid.cse.nagoya-u.ac.jp

https://doi.org/10.1017/jfm.2011.74 Published online by Cambridge University Press

One may then consider at least two factors: one is the nonlinear dynamics due to the convection of fluid under the existence of the Coriolis force, and the other is the linear dynamics due to the Coriolis force, i.e. the linear dynamics of inertial waves. The Coriolis force plays important roles at any time scale in both of the dynamics. The force alters the energy transfer due to the nonlinear convection, although the force produce no energy.

As regards the nonlinear dynamics, it has been argued that the nonlinear energy transfer gives rise to the formation of columnar structures for homogeneous rotating turbulence. The transfer concentrates energy around the plane $k_3 = 0$ in the wave vector space, where k_3 is the wavenumber parallel to the rotation axis. The transfer leads to flow two-dimensionalization. Cambon & Jacquin (1989) showed that the concentration of energy near the $k_3 = 0$ plane yields the columnar eddies in physical space by using axisymmetric spectral formulations of the second-order tensor of velocity. They predicted the transfer towards the $k_3 = 0$ plane by a spectral closure based on eddy-damped quasi-normal Markovian theory, EDQNM2. Waleffe (1993) showed the transfer towards the $k_3 = 0$ plane analytically on the basis of the instability assumption proposed by Waleffe (1992). The transfer was also confirmed for freely decaying turbulence by direct numerical simulation (DNS) (Morinishi, Nakabayashi & Ren 2001; Liechtenstein, Godeferd, & Cambon 2005), large eddy simulation (LES) (Cambon *et al.* 1997) and wave turbulence theory developed in the limit of small Rossby number, Ro, asymptotic quasi-normal Markovian closure (AQNM) (Bellet *et al.* 2006). Here $Ro = U/(2\Omega\mathscr{L})$, Ω is a constant rotation rate, U is the characteristic velocity and $\mathscr{L}$ is the characteristic length. Galtier (2003) confirms incomplete two-dimensionalization almost without an inverse energy cascade, as discussed in Bellet *et al.* (2006).

Bartello *et al.* (1994) and Bourouiba & Bartello (2007) found net energy transfer from three-dimensional modes ($k_3 \neq 0$) to two-dimensional modes ($k_3 = 0$) in numerical simulations of the freely decaying turbulence at moderate Rossby numbers, i.e. Ro ranging from $O(10^{-2})$ to $O(1)$. Hossain (1994), Smith & Waleffe (1999) and Chen *et al.* (2005) observed significant transfer of energy from modes with $k_3 \neq 0$ at intermediate scales to modes with $k_3 = 0$ at larger scales in numerical simulations of the turbulence subjected to intermediate-scale forcing at moderate Ro, $Ro_f = O(10^{-1})$ and $Ro_f = O(10^{-3})$–$O(10^{-1})$, respectively, where $Ro_f = U_f/(2\Omega\mathscr{L}_f)$, $\mathscr{L}_f = 1/k_f$ and $U_f = (\epsilon_f/k_f)^{1/3}$. Here k_f and ϵ_f are the typical wavenumber of the force spectrum and the energy input rate, respectively. Smith & Lee (2005) found that near resonant triad interactions among inertial waves play an important role in the transfer at $Ro_f = O(10^{-1})$.

As regards the linear dynamics in the presence of the Coriolis force, Davidson, Staplehurst & Dalziel (2006) studied rotating turbulence which consists of turbulent and non-turbulent regions and is inhomogeneous in the axial direction. They argued that, in addition to the nonlinear dynamics, the linear dynamics can play an important role in the formation of the columnar structures at least on the linear time scale $1/\Omega$ even when $Ro \sim 1$, i.e. the linear time scale is comparable to the nonlinear time scale $\mathscr{L}/U$. Elongated eddy structures grow into non-turbulent regions in experiments on inhomogeneous rotating turbulence. They found that a characteristic size of the structure in the axial direction grows linearly in terms of time, which is due to the propagation of the linear inertial waves whose group velocity is the fastest in the axial direction. They also presented an example where an initially compact vortex blob in an unbounded domain is elongated in the axial direction by the linear inertial wave propagation in the absence of the nonlinear dynamics. The elongation does not

https://doi.org/10.1017/jfm.2011.74 Published online by Cambridge University Press

accompany the evolution of energy distribution in wavenumber space. Staplehurst, Davidson & Dalziel (2008) conjectured that the above argument about columnar eddy formation in inhomogeneous flow may be extended to the case of homogeneous rotating turbulence.

In an experiment on the transition from a quiescent fluid to turbulence in a rotating tank, Kolvin *et al.* (2009) found that energy is transported in the axial direction by inertial wave packets before nonlinearity essentially starts to work in the energy transfer process.

One may think that the role of the linear dynamics in the formation is less significant for homogeneous rotating turbulence than for rotating flow which is inhomogeneous in the axial direction and consists of turbulent and non-turbulent regions. For inhomogeneous flow, the energy can travel into the non-turbulent regions due to the inertial waves radiated from the turbulent regions, and induce transition from a non-turbulent flow to turbulence. Thus, the size of the turbulent regions in the axial direction may grow linearly in time. In contrast, homogeneous turbulence has many energetic eddies in physical space at large scales. The inertial waves radiated from the eddies can interfere with each other.

The objective of the present paper is to get some quantitative idea of the roles of the linear and the nonlinear dynamics, i.e. the roles of the Coriolis force and nonlinear convection, in the formation of columnar structures in freely decaying homogeneous rotating turbulence within the time period showing the linear growth of size of eddies in terms of time.

Prior to the quantitative analysis of the formation of the columnar structures, it is of interest to define proper measures which well characterize the structures quantitatively. Among candidates for such measures are the integral length scales based on the two-point correlation defined as

$$L^{\beta}(\zeta) = \frac{\displaystyle\int_0^{\infty} \langle \zeta'(\boldsymbol{x}, t)\zeta'(\boldsymbol{x} + r\boldsymbol{i}_{\beta}, t)\rangle \, \mathrm{d}r}{\langle |\zeta'(\boldsymbol{x}, t)|^2 \rangle}, \tag{1.1}$$

where $\boldsymbol{x} = (x_1, x_2, x_3)$ in the Cartesian coordinate system, t is the time, $\zeta' = \zeta(\boldsymbol{x}, t) - \langle \zeta(\boldsymbol{x}, t)\rangle$, $\langle \zeta \rangle$ denotes the volume average of ζ, $\boldsymbol{i}_{\beta}$ is the unit vector in the βth direction and ζ may be any quantity of physical interest, for example, the jth velocity component $u_j(\boldsymbol{x}, t)$ or the jth vorticity component $\omega_j(\boldsymbol{x}, t)$. This length scale with ζ being linear in terms of u_j shows no substantial increase in time in the framework of the linear inviscid theory as is well known (see § 2), although the length scale characterizes the columnar eddy formation due to the nonlinear dynamics. We therefore need to pay some attention to the definition of the measures characterizing the elongation, to examine the role of the linear dynamics in the columnar formation.

A simple example of inviscid linear dynamics of an initially compact eddy in a periodic box suggests a conflict between the use of the length scales, $L^{\beta}(u_j)$ or $L^{\beta}(\omega_j)$, and an intuitive idea obtained from visualization of the flow field (see § 3). The visualization suggests the formation of eddies elongated in the direction parallel to the rotation axis, i.e. the increase of the length scale in this direction. This observation is in agreement with Davidson *et al.* (2006). Such a conflict can be avoided if one uses length scales defined in terms of the two-point correlation of the square of the velocity or vorticity instead of the correlation of the velocity or vorticity.

Section 4 shows DNS results of homogeneous freely decaying rotating turbulence satisfying the Navier–Stokes equations in a periodic box at moderate Rossby numbers.

https://doi.org/10.1017/jfm.2011.74 Published online by Cambridge University Press

In order to understand the roles of the Coriolis force and the nonlinear convection in the Navier–Stokes dynamics, we compare two kinds of turbulent flows in § 5. One is a basic reference field obtained by DNS. The other consists of a series of artificial flows, each of which is obtained by numerical simulation where the nonlinear and viscous terms in the Navier–Stokes equation are switched off at a given instant. It is difficult to perform such an operation in laboratory experiments. In this sense, it is a kind of thought experiment, or a computational surgery. The scale dependence of the roles of the Coriolis force and the convection, and the influences of the domain size and viscosity in DNS are also discussed in § 6. Conclusions are drawn in § 7.

2. Basic equations and linear dynamics

In this paper, we consider the rotating turbulence of an incompressible fluid obeying the Navier–Stokes equation,

$$\frac{\partial \boldsymbol{u}}{\partial t} + 2\boldsymbol{\Omega} \times \boldsymbol{u} + (\boldsymbol{u}\cdot\nabla)\boldsymbol{u} = -\frac{1}{\rho}\nabla p + \nu\nabla^2\boldsymbol{u}, \tag{2.1}$$

and the incompressibility condition

$$\nabla\cdot\boldsymbol{u} = 0, \tag{2.2}$$

in a rotating frame, where $\boldsymbol{u}$ is the velocity field, $\boldsymbol{\Omega}$ is the angular velocity of the system, p is the pressure including the effect of the centrifugal force, ρ is the density of the fluid and ν is the kinematic viscosity. We take the x_3-axis being parallel to $\boldsymbol{\Omega}$, so that $\boldsymbol{\Omega} = \Omega\boldsymbol{i}_3$.

If the nonlinear convection term as well as the viscous term is negligible, (2.1) reduces to the linear equation

$$\frac{\partial \boldsymbol{u}}{\partial t} + 2\boldsymbol{\Omega}\times\boldsymbol{u} = -\frac{1}{\rho}\nabla p. \tag{2.3}$$

The solution satisfying (2.3) under (2.2) can be obtained by various ways. We use the helical decomposition (Cambon & Jacquin 1989; Waleffe 1992; Morinishi *et al.* 2001; Sagaut & Cambon 2008) such as

$$\hat{\boldsymbol{u}}(\boldsymbol{k}, t) = \xi_+(\boldsymbol{k}, t)\boldsymbol{N}(\boldsymbol{k}) + \xi_-(\boldsymbol{k}, t)\boldsymbol{N}(-\boldsymbol{k}), \tag{2.4}$$

where $\hat{\boldsymbol{u}}(\boldsymbol{k}, t)$ is the Fourier representation of $\boldsymbol{u}(\boldsymbol{x}, t)$, $\boldsymbol{k}$ is a wave vector, $\boldsymbol{N}(\boldsymbol{k}) = \boldsymbol{e}^2(\boldsymbol{k}) - \mathrm{i}\boldsymbol{e}^1(\boldsymbol{k})$ and $\boldsymbol{N}^*(\boldsymbol{k}) = \boldsymbol{N}(-\boldsymbol{k})$. The symbol $\boldsymbol{N}^*(\boldsymbol{k})$ expresses the complex conjugate of $\boldsymbol{N}(\boldsymbol{k})$. The Craya–Herring bases $\boldsymbol{e}^1(\boldsymbol{k})$ and $\boldsymbol{e}^2(\boldsymbol{k})$ (Craya 1958; Herring 1974) are defined by

$$\boldsymbol{e}^1(\boldsymbol{k}) \equiv \frac{\boldsymbol{k}\times\boldsymbol{i}_3}{|\boldsymbol{k}\times\boldsymbol{i}_3|}, \qquad \boldsymbol{e}^2(\boldsymbol{k}) \equiv \frac{\boldsymbol{k}\times\boldsymbol{e}^1(\boldsymbol{k})}{|\boldsymbol{k}\times\boldsymbol{e}^1(\boldsymbol{k})|}. \tag{2.5}$$

Expression (2.4) guarantees the solenoidal condition $\boldsymbol{k}\cdot\hat{\boldsymbol{u}}(\boldsymbol{k}, t) = 0$ for any $\xi_\pm$.

The linear equation (2.3) can be solved as

$$\xi_\pm(\boldsymbol{k}, t) = \xi_\pm(\boldsymbol{k}, 0)\,\mathrm{e}^{\pm\mathrm{i}\sigma(\boldsymbol{k})t}. \tag{2.6}$$

Here the wave frequency $\sigma(\boldsymbol{k})$ is given by

$$\sigma(\boldsymbol{k}) = \pm 2\Omega\cos\theta, \tag{2.7}$$

so that the group velocity $\boldsymbol{c}$ is given by

$$\boldsymbol{c}(\boldsymbol{k}) = \pm\frac{2\Omega}{k}(\boldsymbol{i}_3 - \hat{\boldsymbol{k}}\cos\theta), \tag{2.8}$$

https://doi.org/10.1017/jfm.2011.74 Published online by Cambridge University Press

where $\hat{\boldsymbol{k}} = \boldsymbol{k}/k$, $k = |\boldsymbol{k}|$ and θ is the angle between $\boldsymbol{k}$ and $\boldsymbol{\Omega}$. Note that $\boldsymbol{c}(\boldsymbol{k}) \perp \boldsymbol{k}$. The group velocity $\boldsymbol{c}(\boldsymbol{k})$ for a given k is the largest for $\theta = \pi/2$, for which $\boldsymbol{c}(\boldsymbol{k}) \parallel \boldsymbol{i}_3 \perp (k_1, k_2, 0)$, i.e. the inertial wave propagates in the direction perpendicular to the rotation axis.

Let $\hat{Q}_{ij}(\boldsymbol{k})$ be the Fourier transform of the two-point velocity correlation $Q_{ij}(\boldsymbol{r})$ defined as

$$Q_{ij}(\boldsymbol{r}, t) \equiv \langle u_i(\boldsymbol{x} + \boldsymbol{r}) u_j(\boldsymbol{x}, t) \rangle \equiv \int \hat{Q}_{ij}(\boldsymbol{k}, t) \exp(\mathrm{i}\boldsymbol{k} \cdot \boldsymbol{r}) \, \mathrm{d}\boldsymbol{k}, \tag{2.9}$$

where the brackets denote the ensemble average. If the field is periodic in space, then the integral is to be replaced by a discrete sum, and the brackets may be understood as the volume average over $\boldsymbol{x}$.

Using the exact representation of $\hat{Q}_{ij}(\boldsymbol{k}, t)$ in terms of an energy spectrum $e(\boldsymbol{k}, t)$, polarization anisotropy $Z(\boldsymbol{k}, t)$ and a helicity spectrum for any anisotropic flow (Cambon & Jacquin 1989), we have

$$\hat{Q}_{\alpha\alpha}(\boldsymbol{k}, t) = e(\boldsymbol{k}, t) P_{\alpha\alpha} + \mathrm{Re}[Z(\boldsymbol{k}, t) N_\alpha(\boldsymbol{k}) N_\alpha(\boldsymbol{k})], \tag{2.10}$$

where $e(\boldsymbol{k}, t) = \langle |\xi_+(\boldsymbol{k}, t)|^2 \rangle + \langle |\xi_-(\boldsymbol{k}, t)|^2 \rangle$, $Z(\boldsymbol{k}, t) = 2\langle \xi_+(\boldsymbol{k}, t) \xi_-^*(\boldsymbol{k}, t) \rangle$, $P_{\alpha\alpha} = 1 - k_\alpha^2/k^2$ and N_α is an αth component of $\boldsymbol{N}$. The polarization anisotropy $Z(\boldsymbol{k}, t)$ is a complex scalar. Einstein's summation convention is not used for the repeated indices.

Equations (2.4) and (2.6) imply that $\hat{\boldsymbol{u}}(\boldsymbol{k}, t)$ is uniquely determined by the initial data, independently of the data of the other modes. In particular, we have

$$2e(\boldsymbol{k}, t) \equiv \langle |\hat{\boldsymbol{u}}(\boldsymbol{k}, t)|^2 \rangle = \hat{Q}_H(\boldsymbol{k}, t) + \hat{Q}_{33}(\boldsymbol{k}, t) = \text{independent of } t, \tag{2.11}$$

where $\hat{Q}_H(\boldsymbol{k}, t) \equiv \hat{Q}_{11}(\boldsymbol{k}, t) + \hat{Q}_{22}(\boldsymbol{k}, t)$. Thus, as is well known, the kinetic energy of each Fourier (wave vector) mode is conserved, and there is no exchange of energy between different modes, within the inviscid linear dynamics in contrast to the nonlinear Navier–Stokes dynamics.

Substitution of (2.6) into (2.10) gives

$$\hat{Q}_{33}(\boldsymbol{k}, t) = \sin^2\theta \{ e(\boldsymbol{k}, 0) + \mathrm{Re}[Z(\boldsymbol{k}, 0) \exp(\mathrm{i}2\sigma t)] \}, \tag{2.12}$$

$$\hat{Q}_H(\boldsymbol{k}, t) = (1 + \cos^2\theta) e(\boldsymbol{k}, 0) - \sin^2\theta \ \mathrm{Re}[Z(\boldsymbol{k}, 0) \exp(\mathrm{i}2\sigma t)], \tag{2.13}$$

where $Z(\boldsymbol{k}, t) = Z(\boldsymbol{k}, 0) \exp(\mathrm{i}2\sigma t)$.

2.1. *Axisymmetric turbulence*

In axisymmetric turbulence, the statistics depend on $\boldsymbol{k}$ only through k and θ, so that one may write

$$Z(\boldsymbol{k}, t) = Z(k, \cos\theta, t). \tag{2.14}$$

Substitution of (2.12) and (2.13) with (2.14) into (2.9) yields

$$Q_{ij}(\boldsymbol{r}, t) = C_{ij}(\boldsymbol{r}) + D_{ij}(\boldsymbol{r}, t), \tag{2.15}$$

where C_{ij} is time-independent, while D_{ij} is time-dependent. In particular, for $i = j = 3$, we have

$$C_{33}(\boldsymbol{r}) = \int \sin^2\theta \ e(\boldsymbol{k}, 0) \exp(\mathrm{i}\boldsymbol{k} \cdot \boldsymbol{r}) \, \mathrm{d}\boldsymbol{k}, \tag{2.16}$$

$$D_{33}(\boldsymbol{r}, t) = \int \sin^2\theta \ \mathrm{Re}[Z(k, \cos\theta, 0) \exp(\mathrm{i}2\sigma t)] \cos(\boldsymbol{k} \cdot \boldsymbol{r}) \, \mathrm{d}\boldsymbol{k}. \tag{2.17}$$

https://doi.org/10.1017/jfm.2011.74 Published online by Cambridge University Press

The integral (2.17) represents a collection of oscillators with different frequencies. For $t > 0$, it may be regarded as a mixture of oscillators with different phases.

It is shown from (2.15) and (2.17) that

(i) $Q_{33}(\boldsymbol{0}, t) \to$ constant as $t \to \infty$, because of Riemann–Lebesgue's theorem, which says that as $t \to \infty$,

$$\int I_c(x) \cos(xt)\, \mathrm{d}x \;\to\; 0 \quad \text{and} \quad \int I_s(x) \sin(xt)\, \mathrm{d}x \;\to\; 0, \tag{2.18}$$

provided that $I_c(x)$ and $I_s(x)$ are absolutely integrable.

(ii) The integral $\int_0^\infty Q_{33}(r\boldsymbol{i}_3, t)\, \mathrm{d}r$ is time-independent, because $\sin\theta = 1$ and $\cos\theta = \sigma = 0$ at $k_3 = 0$, so that

$$\int_0^\infty D_{33}(r\boldsymbol{i}_3, t)\, \mathrm{d}r = \pi \int \mathrm{Re}[Z(k, 0, 0)]\, \mathrm{d}k_1\, \mathrm{d}k_2. \tag{2.19}$$

To get further insight on the time dependence of $D_{33}(r\boldsymbol{i}_3, t)$, let us consider an example where the dominant contribution to (2.17) comes from the wavenumber range close to k_0, so that one may put $\cos(\boldsymbol{k}\cdot r\boldsymbol{i}_3) \sim \cos(k_0 r \cos\theta)$ in (2.17). Then one has

$$\begin{aligned} D_{33}(r\boldsymbol{i}_3, t) = \int_{-1}^{1} (&\mathrm{Re}[A(s)]\{\cos[(k_0 r + 4\Omega t)s] + \cos[(k_0 r - 4\Omega t)s]\} \\ &- \mathrm{Im}[A(s)]\{\sin[(k_0 r + 4\Omega t)s] - \sin[(k_0 r - 4\Omega t)s]\})\, \mathrm{d}s, \end{aligned} \tag{2.20}$$

where

$$A(s) = \pi(1 - s^2) \int_0^\infty k^2 Z(k, s, 0)\, \mathrm{d}k \qquad (s = \cos\theta). \tag{2.21}$$

Because of (2.18), $D_{33}(r\boldsymbol{i}_3, t) \to 0$ as $|k_0 r - 4\Omega t| \to \infty$, while for $k_0 r \sim 4\Omega t$, one has

$$D_{33}(r\boldsymbol{i}_3, t) \sim \frac{1}{\Omega t} D\left(\frac{k_0 r}{\Omega t}, \Omega t\right), \tag{2.22}$$

as $t \to \infty$, where

$$D(X, \tau) \equiv \int (\mathrm{Re}[A(\tilde{s}/\tau)] \cos[(X - 4)\tilde{s}] + \mathrm{Im}[A(\tilde{s}/\tau)] \sin[(X - 4)\tilde{s}])\, \mathrm{d}\tilde{s}. \tag{2.23}$$

Thus, the location r_m at which $|D_{33}(r\boldsymbol{i}_3, t)|$ takes its maximum as a function of r at large $k_0 r$ travels with the velocity $4\Omega/k_0$, and the height $|D_{33}(r_m\boldsymbol{i}_3, t)|$ decays $\propto (\Omega t)^{-1}$, as $\Omega t \to \infty$, provided that the angular dependence of $A(s)$ is weak, so we may neglect the dependence of A on s in (2.23). This decay and the time independence of (2.19) imply that the typical width of $D_{33}(r\boldsymbol{i}_3, t)$ near the peak grows linearly in time as $t \to \infty$.

According to (2.15), $Q_{33}(r\boldsymbol{i}_3, t)$ is determined by two contributions: one is the C_{33}-term that is time-independent, and the other is the D_{33}-term that is time-dependent. Suppose that $\Omega t/k_0$ is much larger than a characteristic length scale of $C_{33}(r\boldsymbol{i}_3)$, say $\int_0^\infty C_{33}(r\boldsymbol{i}_3)\, \mathrm{d}r / C_{33}(\boldsymbol{0})$. Then at $r \ll \Omega t/k_0$, $Q_{33}(r\boldsymbol{i}_3, t)$ is dominated by the time-independent C_{33}, while at $r \sim \Omega t/k_0$, it is dominated by D_{33}. The asymptotic time dependence of the height and width at $r \sim r_m$ suggests that $D_{33}(r\boldsymbol{i}_3, t)$ can be well scaled by $\tilde{r} \equiv k_0 r/(\Omega t)$, as suggested by Staplehurst *et al.* (2008). If the turbulence is isotropic at an initial instant, then $Z(\boldsymbol{k}, t) = 0$ and $D_{33}(\boldsymbol{r}, t) = 0$. The contribution from D_{33} must therefore be small for initially almost isotropic turbulence.

https://doi.org/10.1017/jfm.2011.74 Published online by Cambridge University Press

One may be interested in defining a measure to quantify the characteristic length scales, such as $L^3(u_3)$ defined by (1.1), i.e.

$$L^3(u_3) = \frac{\displaystyle\int_0^\infty Q_{33}(r\boldsymbol{i}_3, t)\,\mathrm{d}r}{Q_{33}(\boldsymbol{0}, t)}. \tag{2.24}$$

Substitution of (2.15)–(2.17) into (2.24) yields

$$L^3(u_3) = \frac{C_0 + D_0(t)}{Q_{33}(\boldsymbol{0}, t)}, \tag{2.25}$$

where C_0 and D_0 are the integrals of $C_{33}(r\boldsymbol{i}_3)$ and $D_{33}(r\boldsymbol{i}_3, t)$ with respect to r, respectively. In (2.25), not only C_0 but also D_0 are time-independent because of (2.19). The length scale $L^3(u_3)$ defined by (2.24) therefore tends to a constant and shows no temporal growth at large enough t, because as mentioned above, $Q_{33}(\boldsymbol{0}, t) \to$ constant as $t \to \infty$.

One may then consider another length scale such as

$$\mathscr{L}_1^3(u_3) = \left[\frac{\displaystyle\int_0^\infty r\,Q_{33}(r\boldsymbol{i}_3, t)\,\mathrm{d}r}{Q_{33}(\boldsymbol{0}, t)}\right]^{1/2}, \tag{2.26}$$

which was proposed by Staplehurst *et al.* (2008), as a candidate for integral length scales characterizing the elongation of the eddies. This length scale may be written in the form

$$\mathscr{L}_1^3(u_3) = \left[\frac{C_1 + D_1(t)}{Q_{33}(\boldsymbol{0}, t)}\right]^{1/2}, \tag{2.27}$$

where C_1 is time-independent and $D_1(t)$ is given by

$$D_1(t) = \int_0^\infty r\,D_{33}(r\boldsymbol{i}_3, t)\,\mathrm{d}r, \tag{2.28}$$

and may be rewritten as

$$\begin{aligned} D_1(t) &= \lim_{\epsilon\to+0}\int_0^\infty \mathrm{d}r \int \mathrm{d}\boldsymbol{k}\, r\exp\{(-\epsilon + \mathrm{i}k_3)r\}\mathrm{Re}[\tilde{Z}(\boldsymbol{k}, 0)\exp(\mathrm{i}2\sigma t)] \\ &= \mathrm{i}\lim_{\epsilon\to+0}\int_0^\infty \mathrm{d}r \int \mathrm{d}\boldsymbol{k}\exp\{(-\epsilon + \mathrm{i}k_3)r\}\frac{\partial}{\partial k_3}(\mathrm{Re}[\tilde{Z}(\boldsymbol{k}, 0)\exp(\mathrm{i}2\sigma t)]) \\ &= -\lim_{\epsilon\to+0}\int \mathrm{d}\boldsymbol{k}\frac{k_3}{k_3^2 + \epsilon^2}\left(\mathrm{Re}\left[\frac{\partial\tilde{Z}(\boldsymbol{k}, 0)}{\partial k_3}\exp(\mathrm{i}2\sigma t)\right] - 2t\frac{\partial\sigma}{\partial k_3}\mathrm{Im}[\tilde{Z}(\boldsymbol{k}, 0)\exp(\mathrm{i}2\sigma t)]\right), \end{aligned} \tag{2.29}$$

and bounded as

$$\begin{aligned} |D_1(t)| &\leqslant \lim_{\epsilon\to0+}\int \mathrm{d}\boldsymbol{k}\frac{k_3}{k_3^2 + \epsilon^2}\left(\left|\frac{\partial\tilde{Z}(\boldsymbol{k}, 0)}{\partial k_3}\right| + 4\Omega t\frac{k_H^2}{k^3}\left|\tilde{Z}(\boldsymbol{k}, 0)\right|\right) \\ &\propto \widetilde{D}_1 \times \Omega t \quad \text{as } t \to \infty, \end{aligned} \tag{2.30}$$

where $\tilde{Z}(\boldsymbol{k}, 0) = \sin^2\theta Z(\boldsymbol{k}, 0)$, $k_H^2 = k_1^2 + k_2^2$ and $\widetilde{D}_1$ is a constant. Hence, as $t \to \infty$, the growth of the length scale $\mathscr{L}_1^3(u_3)$ defined by (2.26) is at most $\propto (\Omega t)^{1/2}$, rather than $\propto \Omega t$, which one would expect from the velocity $4\Omega/k_0$ of the peak of $|D_{33}(r\boldsymbol{i}_3, t)|$, noted above.

https://doi.org/10.1017/jfm.2011.74 Published online by Cambridge University Press

One may also consider another length scale such as $\mathscr{L}_2^3(u_3)$ defined by

$$\mathscr{L}_2^3(u_3) = \left[\frac{\displaystyle\int_0^\infty r^2 Q_{33}(r\boldsymbol{i}_3, t)\,\mathrm{d}r}{Q_{33}(\boldsymbol{0}, t)} \right]^{1/3}. \tag{2.31}$$

The growth of this length scale $\mathscr{L}_2^3(u_3)$ is at most $\propto (\Omega t)^{2/3}$, rather than $\propto \Omega t$, as $t \to \infty$, because the right-hand side of (2.31) may be rewritten as

$$\int_0^\infty r^2 Q_{33}(r\boldsymbol{i}_3, t)\,\mathrm{d}r = \pi \int \frac{\partial^2}{\partial k_3^2} \hat{Q}_{33}(\boldsymbol{k}, t)|_{k_3=0}\,\mathrm{d}k_1\,\mathrm{d}k_2, \tag{2.32}$$

whose growth is at most $(\Omega t)^2$ as $t \to \infty$.

One may also consider length scales defined by (2.24), (2.26) or (2.31), but with Q_{33} replaced by Q_H. Then one can apply arguments similar to the one presented above.

2.2. *Initially isotropic turbulence*

If the turbulence is isotropic at $t = 0$, then we have $Z(\boldsymbol{k}, 0) = 0$. Equations (2.12) and (2.13) then reduce to

$$\hat{Q}_{33}(\boldsymbol{k}, t) = \sin^2\theta e(\boldsymbol{k}, 0), \tag{2.33}$$

$$\hat{Q}_H(\boldsymbol{k}, t) = (1 + \cos^2\theta) e(\boldsymbol{k}, 0). \tag{2.34}$$

Hence, the length scales $L^3(u_3)$, $\mathscr{L}_1^3(u_3)$ and $\mathscr{L}_2^3(u_3)$ defined by (2.24), (2.26) and (2.31) are time-independent.

3. Elongation of compact eddies by inviscid linear dynamics – measures characterizing the elongation

In order to get some more idea of the evolution of the flow field under the inviscid linear dynamics, we consider here a simple example of the flow field which consists of a periodic array of compact eddies at an initial instant.

Let $\boldsymbol{u}(\boldsymbol{x}, t)$ be the velocity field obeying the linear equation (2.3) under periodic boundary conditions with a fundamental periodic box of size 2π in each Cartesian direction, and

$$\boldsymbol{u}(\boldsymbol{x}, 0) = \exp\left[-\left(x_1^2 + x_2^2 + x_3^2\right)/\delta^2 \right] (\Lambda \boldsymbol{i}_3) \times \boldsymbol{x}, \tag{3.1}$$

in the fundamental periodic domain $-\pi \leqslant x_1, x_2, x_3 < \pi$. Here δ is the representative size of the eddy and Λ is the angular velocity. We put $\delta = 0.2$ and $\Lambda = 5$ here, so that the velocity (3.1) is small enough near the periodic boundary. The choice of the form (3.1) is suggested by Davidson *et al.* (2006), who examined the evolution of a compact eddy of the form (3.1) in the infinite domain $\{\boldsymbol{x} | -\infty < x_1, x_2, x_3 < \infty\}$, and showed that the energy propagation in the direction parallel to the rotating axis due to the inviscid linear dynamics plays a significant role in the formation of elongated vorticity structures.

The evolution of the field $\boldsymbol{u}(\boldsymbol{x}, t)$ can be found numerically without difficulty. Figure 1 shows the isosurfaces of the modulus of vorticity ω at $\Omega t = 0$, 3 and 6. It is seen that the initially compact eddy in figure 1(*a*) is decomposed into two compact blobs in figure 1(*b*). Then, the upper and lower eddies grow especially in the direction parallel to the rotational axis as shown in figure 1(*c*).

These figures suggest that elongated structures are formed by the linear dynamics. One may then wish to characterize the elongation quantitatively. As a measure

https://doi.org/10.1017/jfm.2011.74 Published online by Cambridge University Press

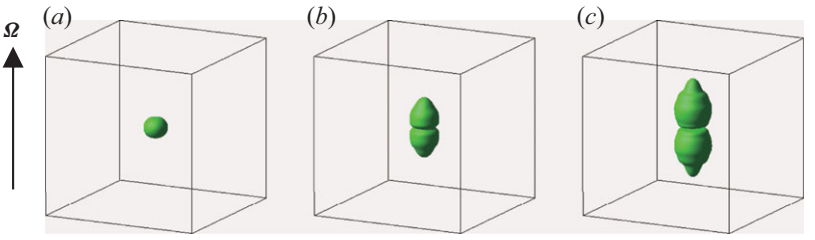


FIGURE 1. (Colour online available at journals.cambridge.org/FLM) Isosurfaces of $\omega = (\omega_j\omega_j)^{1/2}$ with $\omega = m_\omega + 3\sigma_\omega$ at (*a*) $\Omega t = 0$, (*b*) $\Omega t = 3$ and (*c*) $\Omega t = 6$. Here, m_ω and σ_ω are the mean and standard deviation of ω. The arrow illustrates the direction of the rotational axis.

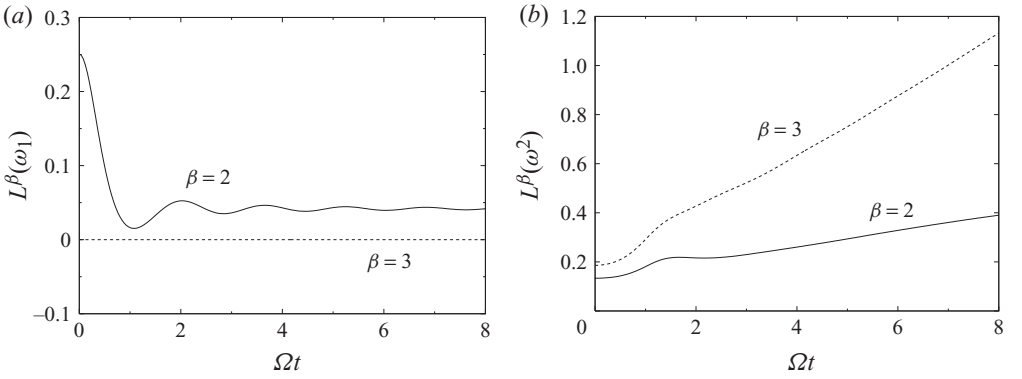


FIGURE 2. Evolution of integral length scales: (*a*) $L^\beta(\omega_1)$ versus Ωt and (*b*) $L^\beta(\omega^2)$ versus Ωt.

characterizing the elongation, one may consider using the integral length scales such as $L^\beta(\zeta)$ defined by (1.1). So far, ζ in the definition of (1.1) may be any quantity of physical interest. It is tempting to put $\zeta = \omega_i$ or u_i. Or one may put ζ as the light intensity of highlighted pearlescence as used in the laboratory experiments by Staplehurst *et al.* (2008).

As ζ, we take $\zeta = \omega_1$ rather than $\zeta = u_1$ here, because the vorticity is often used for visualization of columnar eddies in previous studies (e.g. Bartello *et al.* 1994; Bourouiba & Bartello 2007; Staplehurst *et al.* 2008). Figure 2(*a*) plots the transversal integral length scales $L^2(\omega_1)$ and $L^3(\omega_1)$ versus time. It shows a transient decrease of $L^2(\omega_1)$ at an early period, say $0 < \Omega t \lesssim 1$, but shows no substantial growth of either $L^2(\omega_1)$ or $L^3(\omega_1)$. Such an absence of growth in $L^2(\omega_1)$ and $L^3(\omega_1)$ can be understood by the linear analysis in the previous section, as follows.

The length scales $L^\beta(\omega_1)$ ($\beta = 2, 3$) defined by (1.1) may be written as

$$L^2(\omega_1) = \frac{2\pi}{\langle\omega_1^2\rangle}\int_0^\infty k^3\,\mathrm{d}k\int_{-1}^1 \frac{s^2\,\mathrm{d}s}{(1-s^2)^{1/2}}\{e(k,s,t) - \mathrm{Re}[Z(k,s,t)]\}, \tag{3.2}$$

$$L^3(\omega_1) = \frac{\pi^2}{\langle\omega_1^2\rangle}\int_0^\infty k^3\,\{e(k,0,t) + \mathrm{Re}[Z(k,0,t)]\}\,\mathrm{d}k, \tag{3.3}$$

for axisymmetric turbulence, where $e(\boldsymbol{k},t) = e(k,s,t)$, $s = \cos\theta$ and

$$\langle\omega_1^2\rangle = \pi\int_0^\infty k^4\,\mathrm{d}k\int_{-1}^1 \mathrm{d}s\,\left\{(1+s^2)e(k,s,t) + (1-s^2)\mathrm{Re}[Z(k,s,t)]\right\}. \tag{3.4}$$

https://doi.org/10.1017/jfm.2011.74 Published online by Cambridge University Press

The Fourier representation of $\langle\omega_1(\boldsymbol{x})\omega_1(\boldsymbol{x}+\boldsymbol{r})\rangle$ is given by replacing $e(\boldsymbol{k},t)$ and $Z(\boldsymbol{k},t)$ on the right-hand side of (2.10) with $k^2e(\boldsymbol{k},t)$ and $-k^2Z(\boldsymbol{k},t)$, respectively, because $\mathrm{i}\boldsymbol{k}\times\boldsymbol{N}=k\boldsymbol{N}$.

In our particular example of the initial field (3.1), we have $u_3=0$ at $t=0$. It can then be shown that $L^3(\omega_1)=0$ for any t within the inviscid linear theory (see Appendix A.1). This is consistent with the observation in figure 2(*a*), where $L^3(\omega_1)$ is negligibly small for any t. As regards $L^2(\omega_1)$, both $\langle\omega_1^2\rangle$ and the integral term in (3.2) exhibit damped oscillation, so that $L^2(\omega_1)$ should tend to a constant after a certain transient period in the linear theory (see Appendix A.1). This is consistent with the observation in figure 2(*a*).

Thus, the absence of growth in the integral length scales $L^2(\omega_1)$ and $L^3(\omega_1)$ observed in figure 2(*a*) is consistent with the linear theory. However, such an absence seems to contradict the intuitive impression obtained from figure 1, which suggests the increase of the length scales in the axial direction. These observations have motivated us to seek for another measure to quantitatively characterize the elongation observed in figure 1.

In this regard, it is to be noted that if we use the velocity or its derivative for ζ, then the length scale is uniquely determined only by the second-order moments of the velocity field, i.e. $\hat{Q}_{ij}(\boldsymbol{k},t)$. It is similarly the case if we choose $\zeta=u_i(\boldsymbol{x},t)$. Under certain symmetry, we are often not interested in the non-diagonal element with $i\neq j$. However, $\hat{Q}_{ij}$ for $i=j$ depends only on the amplitude $|\hat{u}_i(\boldsymbol{k})|$ which is invariant to any translation of the wave represented by $\hat{u}_i(\boldsymbol{k})$ $(\equiv|\hat{u}_i(\boldsymbol{k})|\exp\{\mathrm{i}\phi(\boldsymbol{k})\})$. This implies that, as is well known, information on the phase $\phi(\boldsymbol{k})$ is missing in $\hat{Q}_{ij}$ for $i=j$. The phase information is essential in the elongation due to the linear dynamics, because the energy $|\hat{\boldsymbol{u}}(\boldsymbol{k})|^2/2$ is time-independent. This consideration leads us to use some other definition of the length scale which may represent information on the phase.

One of the simplest measures one may consider then is $L^\beta(\zeta)$ with ζ being nonlinear in terms of u_j, which represents the phase information better than any ζ linear in u_j. For example, put $\zeta=\omega^2\equiv\sum_j\omega_j\omega_j$. The numerator in the definition of (1.1) is then an integral of a one-time two-point fourth-order correlation. Figure 2(*b*) plots the time dependence of $L^2(\omega^2)$ and $L^3(\omega^2)$. The figure shows the growth of the length scales $L^2(\omega^2)$ and $L^3(\omega^2)$. The growth of $L^3(\omega^2)$, i.e. the length scale in the axial direction, is seen to be much faster than that of $L^2(\omega^2)$. In the following, we call the faster increase of the length scale under consideration in the axial direction than in the other directions 'selective growth'. The plots in figure 2(*b*) are in agreement with the intuitive impression obtained from figure 1 on the selective growth. The integral length scale $L^3(\omega^2)$ grows almost linearly in time for $\Omega t\gtrsim 2$.

These observations show that the length scales based on a one-time two-point second-order correlation of a vorticity component or a velocity one cannot well represent the elongation in the present linear case. On the other hand, the length scales of ω^2, such as $L^3(\omega^2)$, may represent the elongation well. The example considered in this section suggests the importance of the proper choice of the measure characterizing the formation of elongated structures in rotating turbulence.

4. DNS of homogeneous rotating turbulence

In order to take into account the nonlinear dynamics in the Navier–Stokes equation (2.1), we performed DNS of freely decaying rotating turbulence obeying (2.1) and (2.2).

https://doi.org/10.1017/jfm.2011.74 Published online by Cambridge University Press

	Ω	Initial field	$10^4\nu$	R_L	R_λ	Ro^ω	Ro^L	Ro
Run 2-1	2.0	Ini1	15.0	93.2	48.0	4.48	0.241	0.596
Run 5-1	5.0	Ini1	15.0	93.2	48.0	1.79	9.65×10^{-2}	0.239
Run 10-1	10.0	Ini1	15.0	93.2	48.0	0.90	4.82×10^{-2}	0.119
Run 5-2	5.0	Ini2	20.0	56.6	33.5	1.92	0.148	0.295

TABLE 1. The constant rotation rate Ω and initial Reynolds and Rossby numbers in the DNS of freely decaying homogeneous rotating turbulence. The Rossby number $Ro = U/(2\Omega\mathscr{L})$, where u' and L are taken as U and $\mathscr{L}$, respectively. We set $\ell^B = 2\pi$, $N = 256$ and $k_{max} = 121$, where N is the number of grid points in each direction of the Cartesian coordinates, and k_{max} is the maximum wavenumber retained in the DNS.

4.1. *DNS run parameters*

In the DNS, we assumed periodic boundary conditions and used an alias-free Fourier spectral method and a fourth-order Runge–Kutta method for time marching. As regards the initial field, we used two kinds of statistically quasi-stationary and homogeneous isotropic fields, say Ini1 and Ini2. Some details on how to generate the fields Ini1 and Ini2, as well as their turbulence statistics, are given in Appendix B.

Table 1 presents some key parameters characterizing the initial turbulence statistics of the DNS runs. The time increment is $\Delta t = 2.0 \times 10^{-3}$ in all the runs in table 1. The large-scale Reynolds number R_L and the Taylor micro-scale Reynolds number R_λ are defined by $R_L = u'L/\nu$ and $R_\lambda = u'\lambda/\nu$. Here, $u'^2 = 2E/3$ with E the total kinetic energy, L and λ respectively the integral length scale and Taylor micro-scale defined by

$$L = \pi/(2u'^2)\int_0^{k_{max}} \mathrm{d}k\, E(k)/k, \quad \lambda = (15\nu u'^2/\langle\epsilon\rangle)^{1/2}, \tag{4.1}$$

where $E(k)$ is the energy spectrum, and $\langle\epsilon\rangle$ the mean energy dissipation rate. The Reynolds numbers R_L in table 1 are similar to the Reynolds number $R_b = u'b/\nu$ based on the bar size b in the experiments by Staplehurst *et al.* (2008).

The micro-Rossby number Ro^ω and macro-Rossby number Ro^L are defined by

$$Ro^\omega = \omega/(2\Omega), \quad Ro^L = \langle\epsilon\rangle/(2\Omega E), \tag{4.2}$$

respectively (Cambon *et al.* 1997). The macro-Rossby number Ro^L was first introduced by Cambon & Jacquin (1989). The micro-Rossby number Ro^ω in table 1 is of the order of unity and Ro^L is an order of magnitude smaller than Ro^ω. This implies that the linear Coriolis term and the nonlinear convection term are of comparable order in magnitude to each other. Figure 3 shows the time dependence of the micro-Rossby and Taylor micro-scale Reynolds numbers.

4.2. *Elongation in the axial direction*

Figure 4 shows snapshots of intense vorticity regions in Run 5-1. The isotropic initial field consists of many vortex tubes as seen in figure 4(*a*). Figure 4(*b*) shows the formation of columnar structures at an initial period, while figures 4(*c*) and 4(*d*) show intense vorticity regions at later times. These figures show the growth of elongated structures. The structures are in accordance with previous studies, e.g. figure 4.19 in Sagaut & Cambon (2008).

Figures 5(*a*) and 5(*b*) show the integral length scales $L^2(\omega_1)$ and $L^3(\omega_1)$ versus time. It is seen in each run that

https://doi.org/10.1017/jfm.2011.74 Published online by Cambridge University Press

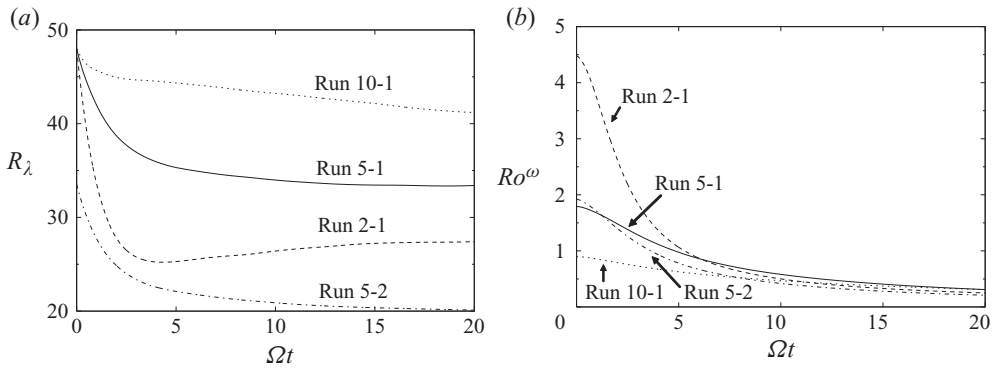


FIGURE 3. (*a*) R_λ versus Ωt and (*b*) Ro^ω versus Ωt.

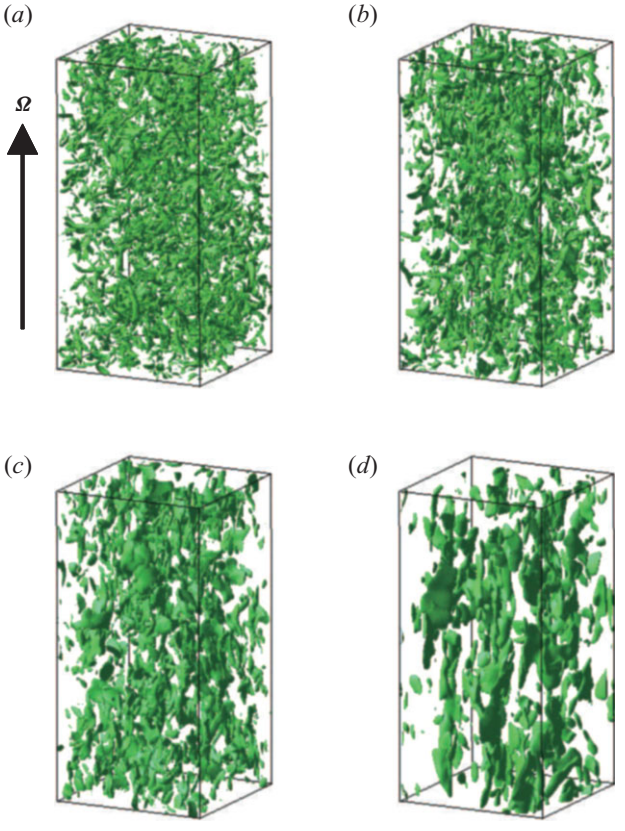


FIGURE 4. (Colour online) Isosurfaces of ω with $\omega = m_\omega + 2\sigma_\omega$ at (*a*) $\Omega t = 0$, (*b*) $\Omega t = 5$, (*c*) $\Omega t = 10$ and (*d*) $\Omega t = 20$ in Run 5-1. A $128 \times 128 \times 256$ rectangular parallelepiped sub-region in each 256^3 cube is visualized.

(i) the integral scales increase approximately linearly in time and
(ii) the increase of $L^3(\omega_1)$ is faster than that of $L^2(\omega_1)$.

The linear growth in time for homogeneous rotating turbulence is consistent with the numerical prediction of EDQNM2 (Cambon & Jacquin 1989), the observations in the laboratory experiments (Jacquin *et al.* 1990; Staplehurst *et al.* 2008), LES (Bartello

https://doi.org/10.1017/jfm.2011.74 Published online by Cambridge University Press

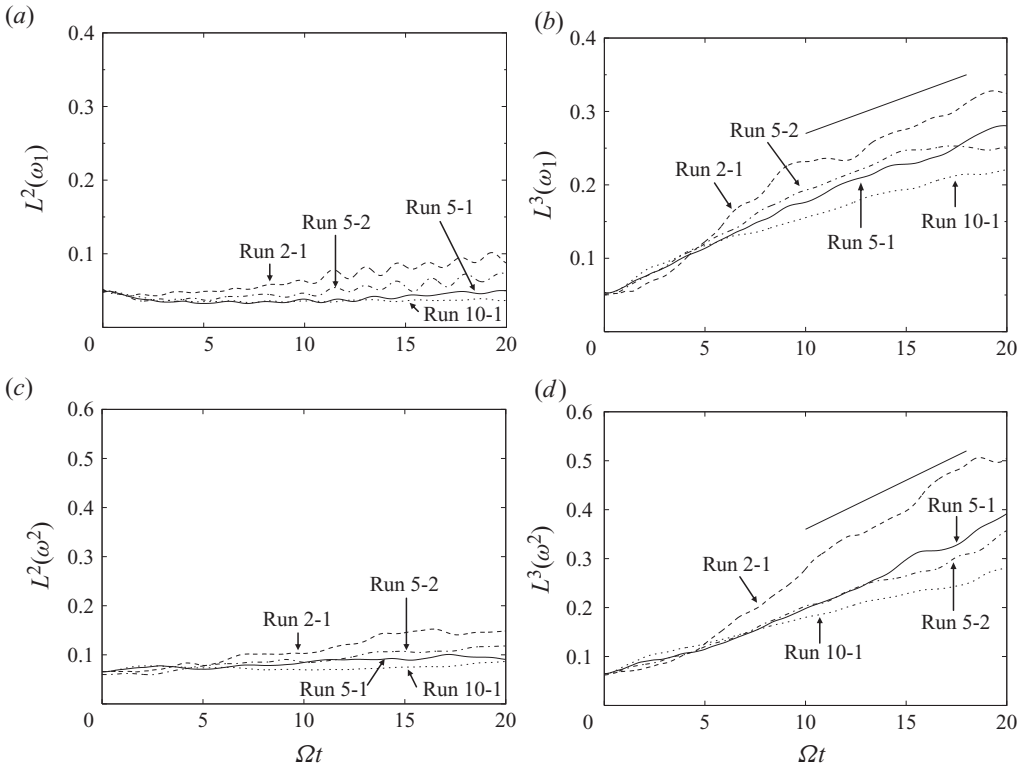


FIGURE 5. (*a*) $L^2(\omega_1)$ versus Ωt, (*b*) $L^3(\omega_1)$ versus Ωt, (*c*) $L^2(\omega^2)$ versus Ωt and (*d*) $L^3(\omega^2)$ versus Ωt.

et al. 1994; Squires *et al.* 1994) and DNS (Bartello *et al.* 1994). The selective growth observed in (ii) is consistent with the understanding that the elongation of the eddies is stronger in the axial direction than in the other directions.

The selective growth is also observed in figures 5(*c*) and 5(*d*) for the integral length scales $L^2(\omega^2)$ and $L^3(\omega^2)$. The difference between the increase of the integral length scales $L^\beta(\omega_1)$ and $L^\beta(\omega^2)$ ($\beta = 2$ or 3) is not so significant in figure 5 for the present nonlinear case of homogeneous turbulence, in contrast to figure 1 for the case of the initially compact eddies discussed in the previous section. The scales $L^2(\omega_1)$ and $L^3(\omega_1)$ can well represent the direction-dependent increase of the length scales in the present case.

One might be interested to see if such a selective growth of $L^3(\omega_1)$ as observed in figure 5(*b*) can be explained by the inviscid pure linear theory. However, it is shown that the length scales $L^\beta(\omega_1)$ ($\beta = 2, 3$) tend to a constant after a certain transient period within the linear theory. In particular, if the turbulence is isotropic, then both $L^2(\omega_1)$ and $L^3(\omega_1)$ must be time-independent within the theory (see Appendix A.2). Thus, the linear theory cannot explain such a growth of $L^3(\omega_1)$ as observed in figure 5(*b*) in initially isotropic turbulence. (The initial field is not exactly isotropic in our DNS, and an inspection in fact shows that $L^2(\omega_1)$ and $L^3(\omega_1)$ under the inviscid linear dynamics with the initial condition used in our DNS are not exactly time-independent, but the time dependence was confirmed to be not significant.)

It is seen in figure 5(*b*) that the growth rates in all the runs averaged over an appropriate time interval, say $5 \lesssim \Omega t \lesssim 20$, are similar to each other. This implies that

https://doi.org/10.1017/jfm.2011.74 Published online by Cambridge University Press

if we plot the length scales normalized by a certain length scale b' versus the time $\Omega(t-t_0)b'$, then the curves overlap each other well, where t_0 is a virtual origin of time.

Such an overlap can be obtained if the two-point correlation function $G(r) \equiv \langle \omega_1(\boldsymbol{x}+r\boldsymbol{i}_3)\omega_1(\boldsymbol{x})\rangle / \langle \omega_1(\boldsymbol{x})^2\rangle$ is of the form $F(r/(\Omega b'(t-t_0))$. Such a function form is compatible with the linear theory for large enough r and Ωt not for small r as discussed in § 2 and in Staplehurst *et al.* (2008) (see also their figures 6 and 7). Their laboratory experiments give a good overlap of the curves of $G(r)$ versus $r/(2\Omega b'(t-t_0))$ from small r to large enough r, though there is more or less scatter of the data for the normalized function, and the collapse is not perfect (see figure 17 in Staplehurst *et al.* 2008). However, the overlap does not necessarily imply that the growth of the length scale in the axial direction $L^3(\omega_1)$ is due to the pure linear dynamics. In fact, as we have seen above, the integral length scale $L^3(\omega_1)$ would not grow substantially within the linear theory, in contrast to the growth observed in figure 5(b). The nonlinear dynamics is therefore indispensable for the growth.

4.3. *Evolution of the anisotropic energy spectrum*

In this respect, it may be interesting to see the distribution of the energy among different Fourier modes, which may change in time by the nonlinear dynamics, in contrast to the linear dynamics. For this purpose, taking into account the axisymmetry of the statistics, let us introduce the spectrum $E(k,\theta)$ defined by

$$E(k,\theta_m) = \frac{1}{4\sin(\theta_m - \Delta\theta/2)\sin(\Delta\theta/2)} \sum_{\Delta} |\hat{\boldsymbol{u}}(\boldsymbol{q})|^2, \tag{4.3}$$

where $\sum_{\Delta}$ denotes the summation with respect to $\boldsymbol{q}$ over the domain $k-1/2 \leqslant |\boldsymbol{q}| < k+1/2$, $\theta_m - \Delta\theta \leqslant \theta < \theta_m$, in which θ is the angle between $\boldsymbol{q}$ and $\Omega\boldsymbol{i}_3$. The spectrum $E(k,\theta_m)$ may be regarded as the average of $|\hat{\boldsymbol{u}}(\boldsymbol{q})|^2/2$ over the domain. Note that one may put $0 \leqslant \theta_m \leqslant \pi/2$ without loss of generality, because the reality condition gives $\hat{\boldsymbol{u}}^*(-\boldsymbol{k}) = \hat{\boldsymbol{u}}(\boldsymbol{k})$, where $\hat{\boldsymbol{u}}^*(\boldsymbol{k})$ is the complex conjugate of $\hat{\boldsymbol{u}}(\boldsymbol{k})$.

Figure 6 shows the spectra $E(k,\theta_m)$ in Run 5-1 at $\Omega t = 0, 5, 10$ and 20, with $\theta_m = m\pi/8$ $(m = 1, 2, 3, 4)$ and $\Delta\theta = \pi/8$. In isotropic turbulence, $E(k,\theta)$ must be independent of θ within the numerical accuracy and statistical fluctuation. This is consistent with figure 6(a), which shows the spectra $E(k,\theta_m)$ of the almost isotropic initial state at $t = 0$. The four curves overlap each other well except at very low k, where the number of modes in each average domain is so small that the statistical fluctuation is not negligible.

According to the inviscid linear theory, the spectrum must be time-independent as discussed in § 2. However, figure 6 shows that the spectrum is time-dependent in our DNS. Figure 6(b,c,d), shows that $E(k,\theta_m)$ is larger than $E(k,\theta_{m-1})$ $(m = 2, 3, 4)$, and the difference between them monotonically increases with time, in almost the entire wavenumber range. In figure 6(d) for $\Omega t = 20$, $E(k,\theta_4)$ is seen to be about an order of magnitude larger than $E(k,\theta_1)$ at $k \sim 10$, where $\theta_4 = \pi/2$ and $\theta_1 = \pi/8$.

These observations are in accordance with the argument that the nonlinear dynamics brings about energy transfer towards the plane $k_3 = 0$. Similar angular-dependent spectra were obtained by EDQNM2 (Cambon & Jacquin 1989; Cambon *et al.* 1997), LES (Cambon *et al.* 1997), DNS (Morinishi *et al.* 2001; Liechtenstein *et al.* 2005) and AQNM (Bellet *et al.* 2006). The results by Liechtenstein *et al.* (2005) for the pure rotating turbulence are shown in figure 4.17 of Sagaut & Cambon (2008).

The modulation of nonlinearity due to the Coriolis force at any Ro, e.g. the anisotropic energy transfer, is represented by the factor $\exp[\mathrm{i}\{\gamma\sigma(\boldsymbol{k}) + \gamma'\sigma(\boldsymbol{p}) +$

https://doi.org/10.1017/jfm.2011.74 Published online by Cambridge University Press

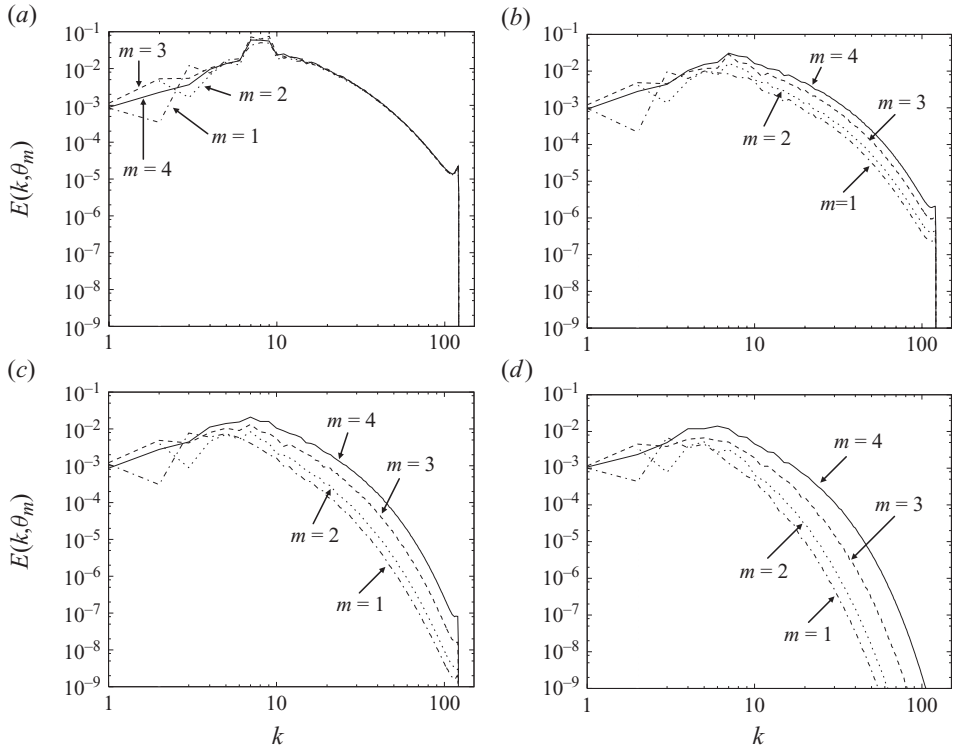


FIGURE 6. Directional energy spectra $E(k,\theta)$ in Run 5-1. (*a*) $\Omega t = 0$, (*b*) $\Omega t = 5$, (*c*) $\Omega t = 10$ and (*d*) $\Omega t = 20$.

$\gamma''\sigma(\boldsymbol{q})\}t]$ ($\gamma, \gamma', \gamma'' = \pm 1$), in the equations governing the evolutions of $e(\boldsymbol{k}, t)$ and $Z(\boldsymbol{k}, t)$ (Cambon & Jacquin 1989).

4.4. *Asymmetry in vorticity statistics*

The existence of the Coriolis force not only brings about the anisotropic growth of the integral scales but also influences the other statistics. For example, reflecting the parity breaking, the Coriolis force may strongly influence the asymmetry between the cyclonic and anti-cyclonic vorticity. One of the simplest measures characterizing the asymmetry is given by the skewness factor $S(\omega_3)$ of axial vorticity defined by

$$S(\omega_3) = \frac{\langle \omega_3^3 \rangle}{\langle \omega_3^2 \rangle^{3/2}} \tag{4.4}$$

(Bartello *et al.* 1994). In reflection-invariant turbulence, the skewness must be zero. In this subsection, we discuss the evolution of $S(\omega_3)$ in our DNS, which gives some idea of the characteristic time scales of the buildup of $S(\omega_3)$ and the formation of columnar structures.

Figure 7 shows the time dependence of $S(\omega_3)$, where $S(\omega_3) \sim 0$ at $t = 0$ because the initial fields are almost isotropic. One can see the following in the figure:

(i) $S(\omega_3)$ grows rapidly at an initial period, say $\Omega t \lesssim 5$, and then saturates to an almost constant value in each run.

(ii) $S(\omega_3)$ at the later period, $\Omega t \gtrsim 5$, is larger for larger R_λ.

(iii) $S(\omega_3)$ at the later period in Run 5-1 is not very different from Run 2-1.

https://doi.org/10.1017/jfm.2011.74 Published online by Cambridge University Press

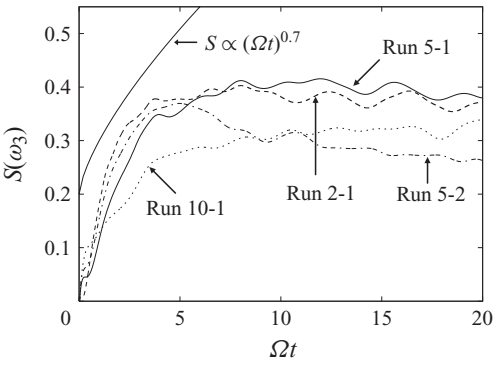


FIGURE 7. $S(\omega_3)$ versus Ωt.

The rapid growth in (i) is in accordance with the laboratory experiments by Morize, Moisy & Rabaud (2005), Staplehurst *et al.* (2008), Moisy *et al.* (2011) and with DNS by van Bokhoven *et al.* (2008), which suggested that, in the initial period, $S(\omega_3)$ grows approximately as $S(\omega_3) \propto (\Omega t)^n$ with $n \sim 0.7$. Gence & Frick (2001) and van Bokhoven *et al.* (2008) showed that the skewness of the longitudinal velocity derivative of the initial homogeneous isotropic field causes this rise. Observation (ii) is consistent with that in van Bokhoven *et al.* (2008). Observation (iii) suggests that in an appropriate Ro^ω range, $S(\omega_3)$ at the later period depends only weakly on Ro^ω. One might think that (iii) is different from the argument by van Bokhoven *et al.* (2008), which concluded that $S(\omega_3)$ at the later period is lower for higher Ω, i.e. lower Ro^ω. However, the difference is not surprising, if we take into account that the conclusion in van Bokhoven *et al.* (2008) is drawn from four DNS with initial $Ro^\omega \simeq 5.46, 1.08, 0.542$ and 0.275, while the initial Rossby numbers Ro^ω in Runs 5-1 and 2-1 are between 5.46 and 1.08 (see table 1). The difference implies the weak Ro^ω dependence of $S(\omega_3)$ at the later period around $Ro^\omega = O(1)$.

Comparison of figures 5 and 7 shows that significant anisotropic eddy elongation showing the linear growth in time of the integral length scales takes place soon after the growth of $S(\omega_3)$. This is consistent with the experimental observations by Staplehurst *et al.* (2008).

5. Role of the Coriolis force versus nonlinear dynamics

In order to understand the role of a certain effect in a phenomenon, it is often instructive to consider a system in the absence of the other effects, and to compare it with the original system. In this section, we consider the role of the Coriolis force by comparing the systems with and without the convection and viscous effects. For this purpose, we simulated the turbulence field in the same way as in Run 5-1 up to a certain time, say t_n, and then suddenly switched off the nonlinear convection and the viscous terms. The operation is a kind of computational surgery. In Runs Lin A, Lin B, Lin C and Lin D reported below, we put $\Omega t_n = 2.5, 5, 10$ and 15, respectively (see table 2). (In practice, we need not and in fact did not repeat Run 5-1 up to the time t_n in each run.) These fields at Ωt_n are anisotropic. The anisotropy is stronger for larger Ωt_n.

Figures 4 and 7 suggest that (i) at the time given by $\Omega t = 5$ or earlier, the field is premature in the sense that either the elongation or the alignment of the eddies in the axial direction is not yet so strong (figure 4*b*), and the skewness factor $S(\omega_3)$ is still at a stage of transient growth (figure 7), while (ii) after $\Omega t = 5$, the field is mature in

https://doi.org/10.1017/jfm.2011.74 Published online by Cambridge University Press

	Initial field	Ro^{ω}
Lin A	Run 5-1 at $\Omega t_n = 2.5$	1.38
Lin B	Run 5-1 at $\Omega t_n = 5$	0.975
Lin C	Run 5-1 at $\Omega t_n = 10$	0.581
Lin D	Run 5-1 at $\Omega t_n = 15$	0.407

TABLE 2. Initial fields of (2.3) with (2.2) and the corresponding Ro^{ω}.

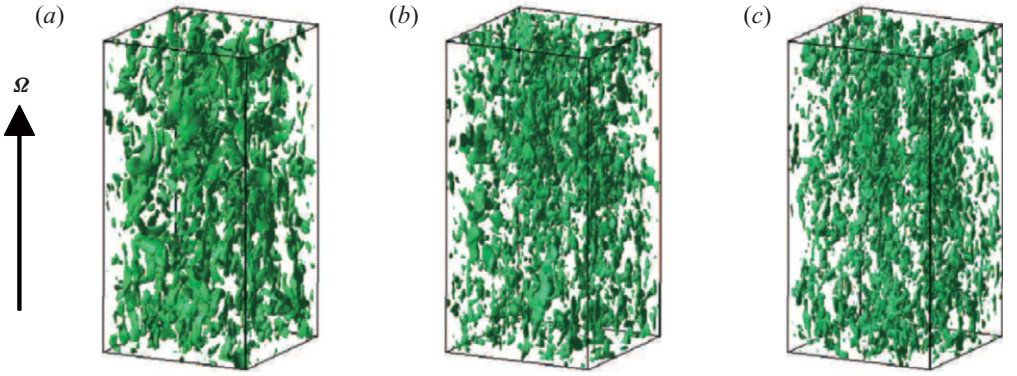


FIGURE 8. (Colour online) Isosurfaces of ω with $\omega = m_\omega + 2\sigma_\omega$ at (*a*) $\Omega t = 12$, (*b*) $\Omega t = 15$ and (*c*) $\Omega t = 20$ in Lin C. A $128 \times 128 \times 256$ rectangular parallelepiped sub-region in each 256^3 cube is visualized.

the sense that eddies are already well elongated and aligned in the direction parallel to the rotation axis, and $S(\omega_3)$ has saturated. Thus, the convection effect is switched off in the premature stage in Lin A and Lin B, but in the mature stage in Lin C and Lin D.

Figure 8 shows snapshots of the vorticity field at $\Omega t = 12, 15$ and 20 in Lin C, which are to be compared with the field at the switch-off time $\Omega t_n = 10$ in figure 4(*c*). The elongation of the eddies is seen to be stronger in figure 8(*a*) ($\Omega t = 12$) than in figure 4(*c*) ($\Omega t = 10$). However, the comparison of figures 8(*b*) and 8(*c*) suggests that there is no further elongation with the increase of time $\Omega(t - t_n)$ after a certain time.

The plots in figure 9 are in accordance with this observation. The figure shows that after a short transient period, the length scales $L^2(\omega^2)$ and $L^3(\omega^2)$ start to decay. During the transition period, the length scales $L^2(\omega^2)$ and $L^3(\omega^2)$ still keep increasing; however the increase with time, especially that of $L^3(\omega^2)$, markedly slows down, and eventually starts to decay, i.e. without the nonlinear dynamics the field cannot sustain the increase of the length scale in the axial direction. The transient period is seen to be shorter for the later switch-off time t_n; it is $0 < \Omega(t - t_n) \lesssim 3$ for Lin A, and $0 < \Omega(t - t_n) \lesssim 2$ for Lin B, Lin C and Lin D. After the transient period, both of the length scales $L^2(\omega^2)$ and $L^3(\omega^2)$ decrease with time almost monotonically.

These slowdowns of the increase in the transient period and eventual decrease suggest the importance of the nonlinear dynamics for sustaining the elongation or the increase of the length scale in the axial direction, at least in the present case of initially homogeneous turbulence. The Coriolis force, if on its own is not sufficient to sustain the elongation.

https://doi.org/10.1017/jfm.2011.74 Published online by Cambridge University Press

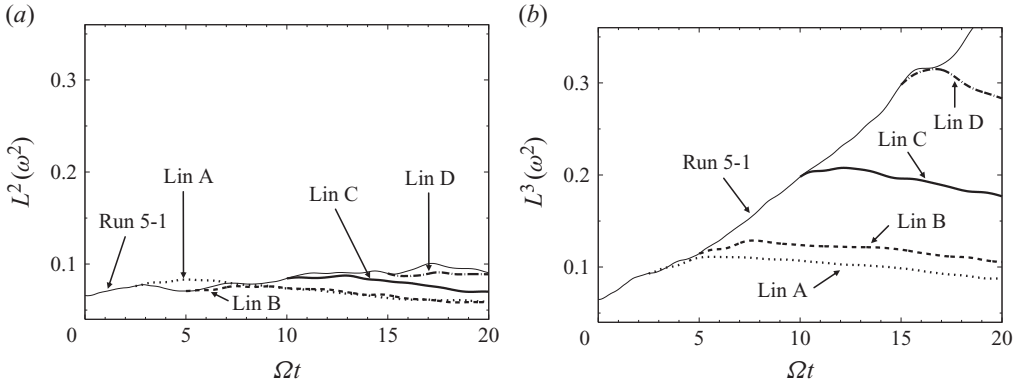


FIGURE 9. (*a*) $L^2(\omega^2)$ versus Ωt and (*b*) $L^3(\omega^2)$ versus Ωt in Lin A, Lin B, Lin C and Lin D (see table 2).

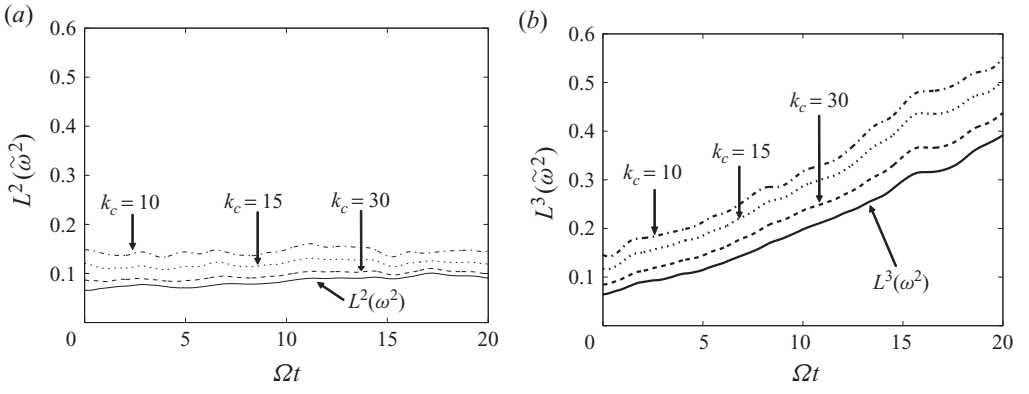


FIGURE 10. (*a*) $L^2(\tilde{\omega}^2)$ versus Ωt and (*b*) $L^3(\tilde{\omega}^2)$ versus Ωt in Run 5-1. The solid curves in (*a*) and (*b*) show the evolutions of $L^2(\omega^2)$ and $L^3(\omega^2)$ in Run 5-1, respectively.

If we switch off the Coriolis force instead of the convection and viscous terms in (2.1) at $\Omega t_n = 10$ in Run 5-1, the difference between $L^3(\omega^2)$ and $L^2(\omega^2)$ tends to be negligible with $\Omega(t - t_n)$ (figure omitted), i.e. recovery to isotropy is observed.

6. Discussion

6.1. *Scale dependence*

The relative importance of the rotation as compared to the nonlinear convection may depend on the scale. To get some idea of its scale dependence, let us introduce the Gaussian filter given by

$$\hat{G}(\boldsymbol{k}) = \exp\left(-\frac{\Delta^2}{24}k^2\right), \quad \Delta = \frac{\pi}{k_c}, \tag{6.1}$$

which is a low-pass filter and one of the most popular filters used in study of LES. The large-scale filtered vorticity field $\tilde{\omega}_j(\boldsymbol{x})$ is defined as the inverse Fourier transform of $\hat{G}(\boldsymbol{k})\hat{\omega}_j(\boldsymbol{k})$.

Figure 10 presents the length scales $L^2(\tilde{\omega}^2)$ and $L^3(\tilde{\omega}^2)$ versus time for $k_c = 10$, 15 and 30 in Run 5-1, where $\tilde{\omega}^2 = \sum_j \tilde{\omega}_j \tilde{\omega}_j$. One can see the following:

(i) the length scales are larger for smaller k_c;

https://doi.org/10.1017/jfm.2011.74 Published online by Cambridge University Press

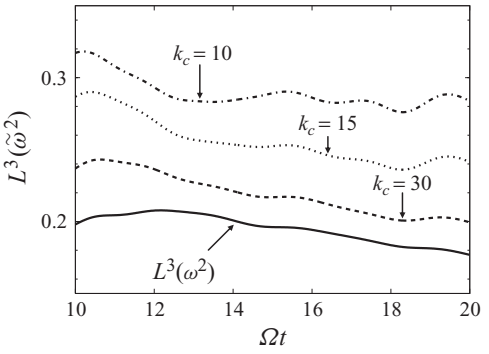


FIGURE 11. $L^3(\tilde{\omega}^2)$ versus Ωt in Lin C. The solid curve shows the evolution of $L^3(\omega^2)$ in Lin C.

(ii) the increase of the integral scale $L^3(\tilde{\omega}^2)$ is much faster than that of $L^2(\tilde{\omega}^2)$ for each k_c,

(iii) but their growth rates are insensitive to k_c.

Observation (i) could be expected because of the nature of filtering which filters out the small scales. Observation (ii) implies that the selective growth, i.e. the faster growth of the length scale in the axial direction than in the other directions, occurs not only at small scales but also at large scales, and (iii) implies that the growth rate is insensitive to the scale in the case considered here.

Figure 11 shows the length scale $L^3(\tilde{\omega}^2)$ versus time for $k_c = 10$, 15 and 30 in Lin C after $\Omega t = 10$. The larger $L^3(\tilde{\omega}^2)$ for smaller k_c is seen for Lin C after the switch-off of the convection effect. It is also seen that the decrease after the switch-off seems to be not sensitive to the cutoff wavenumber k_c, except that the transient period just after the switch-off and before hitting the first peak of $L^3(\tilde{\omega}^2)$ is shorter for smaller k_c. It is similarly the case in the other cases listed in table 2. This suggests that the relative influence of the nonlinear dynamics as compared to the linear dynamics remains longer at larger scales.

In defining the length scale given by (1.1), one might be interested in using quantities other than the vorticity field as ζ, for example, $\zeta = u^2$ or $\zeta = s^2$, where $u^2 = \sum_j u_j u_j$, $s^2 = \sum_{ij} s_{ij} s_{ij}$ and $s_{ij} = (\partial u_i/\partial x_j + \partial u_j/\partial x_i)/2$. We confirmed in our DNS that the length scales $L^\beta(u^2)$ ($\beta = 2, 3$) evolve similarly to $L^\beta(\tilde{\omega}^2)$ with small k_c, while $L^\beta(s^2)$ evolves similarly to $L^\beta(\omega^2)$, in the sense of the selective growth in the presence of the nonlinearity in Run 5-1 and the decay of the length scales after their transient growth in the absence of the nonlinearity in Lin C. The observation is not surprising, if one takes into account that the dominant contribution to ω^2 and s^2 comes from the high wavenumbers or small scales, whereas that to u^2 and $\tilde{\omega}^2$ with low k_c comes from low wavenumbers or large scales.

6.2. *Influence of box size*

As we have seen, the eddies are generally elongated in the axial direction in rotating turbulence, whereas our DNS is based on the use of periodic boundary conditions. It is then natural to ask about the possible influence of the size of the periodic box. In this regard, it is to be noted first that the length scales observed in the figures in the discussions so far are at most about 0.5 (see figures 5, 9, 10 and 11), and they are

https://doi.org/10.1017/jfm.2011.74 Published online by Cambridge University Press

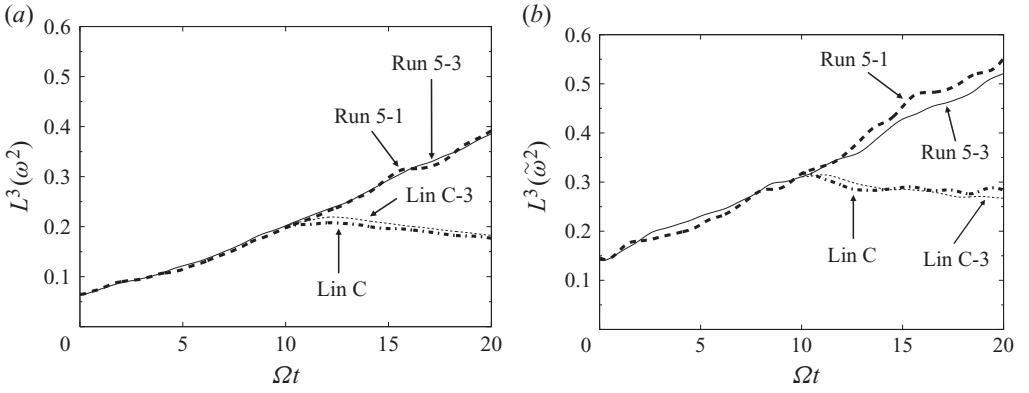


FIGURE 12. (*a*) $L^3(\omega^2)$ versus Ωt and (*b*) $L^3(\tilde{\omega}^2)$ for $k_c = 10$ versus Ωt in Run 5-1, Run 5-3, Lin C and Lin C-3.

therefore much smaller than the fundamental periodic length 2π. This suggests that the influence of the box size is small.

In order to confirm this more clearly, we performed a run, say Run 5-3, under the same condition as Run 5-1, except that the box size $\ell^B = 4\pi$, the number of grid points $N^3 = 512^3$ and the initial field is Ini3 instead of Ini1 (see table 3 in Appendix B). We also performed a run where we switched off the nonlinear and viscous terms at $\Omega t = 10$ in Run 5-3. Here this run is called Lin C-3.

Figure 12(*a*) shows $L^3(\omega^2)$ versus time in Run 5-1, Lin C, Run 5-3 and Lin C-3. The length scales in Run 5-1 are seen to be close to those in Run 5-3. The existence of the small difference between them is not surprising in view of the difference between the initial fields Ini1 and Ini3 used in Runs 5-1 and 5-3, respectively. Although the statistical properties of these fields are very close to each other as shown in table 3, the fields are not exactly the same as each other. The smallness of the difference between Runs 5-1 and 5-3, as well as between Lin C and Lin C-3, regarding $L^3(\omega^2)$, justifies our expectation that the influence of the box size is not significant at least for the length scales in the case considered here.

Figure 12(*b*) is the same as figure 12(*a*), but for $L^3(\tilde{\omega}^2)$ instead of $L^3(\omega^2)$. Again the difference between the runs with different box sizes is seen to be small for the filtered field. This also justifies our expectation of the smallness of the influence of the box size.

6.3. *Influence of viscosity*

One may also be interested in the possible role of viscosity. In order to get some idea of its role, we performed DNS of turbulence which is the same as Run 5-1 until the time given by $\Omega t = 10$, but the nonlinearity is then switched off. Hence, after $\Omega t = 10$, the simulated field obeys the linear viscous dynamics:

$$\frac{\partial \boldsymbol{u}}{\partial t} + 2\boldsymbol{\Omega} \times \boldsymbol{u} = -\frac{1}{\rho}\nabla p + \nu \nabla^2 \boldsymbol{u}, \tag{6.2}$$

and the incompressible condition (2.2).

Figure 13(*a*) plots $L^\beta(\omega^2)$ versus time. One observes that after a transient stage of approximately $10 < \Omega t \lesssim 12$, both of the integral scales $L^3(\omega^2)$ and $L^2(\omega^2)$ show gradual growth whose rates are similar to each other. This observation is consistent

https://doi.org/10.1017/jfm.2011.74 Published online by Cambridge University Press

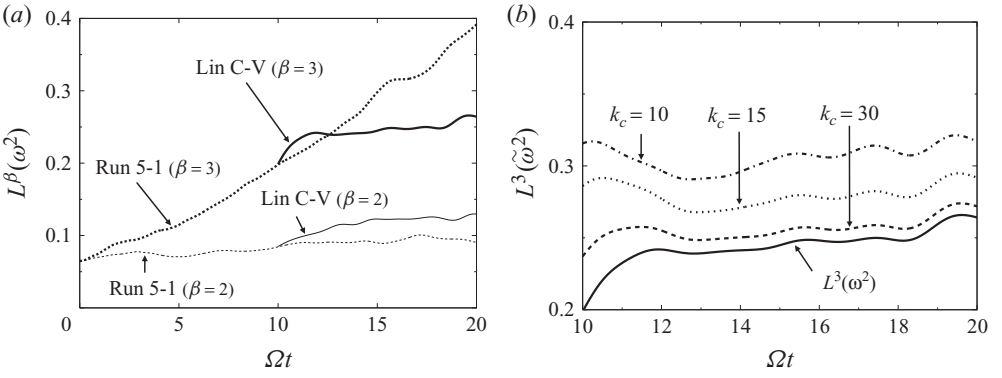


FIGURE 13. (*a*) $L^\beta(\omega^2)$ ($\beta = 2, 3$) versus Ωt in Run 5-1 and Lin C-V. (*b*) $L^3(\tilde{\omega}^2)$ versus Ωt in Lin C-V. The solid curve in (*b*) shows the evolution of $L^3(\omega^2)$ in Lin C-V.

with the conjecture that the viscosity kills the small scales, and it results in the growth of the characteristic length scales.

Figure 13(*b*) plots $L^3(\tilde{\omega}^2)$ versus Ωt. The length scales are seen to be larger for smaller k_c as could be expected. The time dependence is seen to be not sensitive to k_c, although there is a certain difference immediately after the switch-off time: the period before hitting the first peak is shorter for larger k_c.

7. Conclusion

In this paper, we have considered three kinds of rotating flows. (A) One is a flow governed by the inviscid linear dynamics and its initial field consists of a periodic array of compact eddies, and (B) another is a series of freely decaying homogeneous rotating turbulent flows at $Ro \sim 1$ governed by the nonlinear Navier–Stokes dynamics and the initial fields are statistically almost homogeneous and isotropic. The flows in (B) are obtained by DNS and compared with the other kind of flows (C), which are generated by a series of numerical simulations with the same conditions as in (B), but in each of the simulations, nonlinear and viscous terms are switched off at a particular instant.

As regards case (A), the visualization of the flow field shows the formation of columnar structures elongated in the direction parallel to the axis of the system rotation, x_3-axis. However, the length scales $L^\beta(\zeta)$ defined by (1.1) turned out to be unsuitable for representing the elongation, if ζ is a linear functional of the velocity field. This is consistent with the time independence of the energy spectrum. On the other hand, if ζ is nonlinear such as $\zeta = \omega^2$ in the velocity field, the length scale $L^\beta(\zeta)$ can well represent the elongation. The length scale $L^3(\omega^2)$ grows linearly in time. Thus, we reach two different conclusions for the same phenomenon. The difference is due to the difference of the definition of the length scales. This example suggests the importance of recognizing the possibility of the dependence of the 'conclusion' on the definition, as well as the importance of the proper choice of the length scale to quantitatively represent the process of the formation of the columnar structures.

As regards case (B), in contrast to case (A), not only $L^\beta(\omega^2)$ but also $L^\beta(\omega_1)$ can well represent the elongation process and the selective growth in the direction parallel to the rotation axis. We observed the anisotropic evolution of the spectrum due to the anisotropic energy transfer in wavenumber space towards the $k_3 = 0$ plane. Both of the integral length scales in the axial direction exhibit linear growth in time. Neither

https://doi.org/10.1017/jfm.2011.74 Published online by Cambridge University Press

the selective growth of $L^{\beta}(\omega_1)$ nor the anisotropic evolution of the spectrum observed in the DNS can be explained by the inviscid pure linear theory. It is confirmed that the linear growth in time of $L^3(\omega_1)$ is due to the nonlinear dynamics. The comparison of (B) with (C) shows that, without the nonlinear convection effect, the Coriolis force cannot sustain the increase of the length scale $L^3(\omega^2)$ in the direction parallel to the rotation axis. Therefore, the linear growth of $L^3(\omega^2)$ in terms of time is caused by the nonlinearity under the Coriolis force. The scale dependence of the integral scale of the filtered vorticity field $\tilde{\omega}_j$ was examined by using the Gaussian low-pass filter. The linear growth of $L^3(\tilde{\omega}^2)$ in time is insensitive to the scale for the flow (B) obtained by DNS. The growth of $L^3(\tilde{\omega}^2)$ cannot be sustained without the nonlinear convection effect. The lack of substantial growth is also confirmed to be insensitive to the scale, box size and viscosity at least in the case studied in this paper.

Reflecting the parity breaking, the Coriolis force strongly influences the asymmetry between the cyclonic and the anti-cyclonic vorticity. The DNS suggests that the skewness $S(\omega_3)$ of the axial component of vorticity rapidly grows at an initial transient stage, and significant anisotropic eddy elongation showing the linear growth in time of the integral length scales takes place soon after the growth of $S(\omega_3)$.

It would be interesting to characterize the role of the linear inertial waves in the columnar eddy formation under nonlinearity in physical space. However, this is beyond the scope of the present work.

The authors are grateful to P. A. Davidson for fruitful discussions and suggestions throughout this work. They thank C. Cambon for valuable discussions and comments including those on the e–Z decomposition to simplify the equations regarding second-order correlation functions. Y.K. is also grateful to P. Bartello for stimulating discussions during his participation in a program on turbulence at the Issac Newton Institute, Cambridge, in 2008. The computations were carried out on the FX1 system at the Information Technology Center of Nagoya University. This work was supported by the Japan Society for the Promotion of Science (JSPS) Japan-United Kingdom Bilateral Joint Projects, the Grant-in-Aid for Scientific Research (B) 20340099, the Grant-in-Aid for Scientific Research (S) 20224013 from JSPS, and the Grant-in-Aid for Young Scientists (B) 20760055 of the Ministry of Education, Culture, Sports, Science and Technology.

Appendix A. Time dependence of $L^{\beta}(\omega_1)$ in the inviscid linear theory

The denominators $\langle\omega_1^2\rangle$ of (3.2) and (3.3) can be expressed in terms of $e(\boldsymbol{k},0)$ and $Z(\boldsymbol{k},0)$ in the inviscid theory. We have

$$\langle\omega_1^2\rangle = \pi\int_0^\infty k^4\,\mathrm{d}k\int_{-1}^{1}\mathrm{d}s\{(1+s^2)e(k,s,0)+(1-s^2)\mathrm{Re}[Z(k,s,0)\exp(\mathrm{i}4\Omega st)]\}. \quad (A\,1)$$

From Riemann-Lebesgue's theorem, the second term on the right-hand side tends to 0, as $t\to\infty$.

A.1. *Flow under initial condition (3.1)*

Since $e(\boldsymbol{k},0)+\mathrm{Re}[Z(\boldsymbol{k},0)]=0$ for the initial condition (3.1) and $\sigma=0$ for $k_3=0$, (3.3) implies $L^3(\omega_1)=0$ for any t within the linear theory. As regards (3.2),

$$L^2(\omega_1)=\frac{2\pi}{\langle\omega_1^2\rangle}\int_0^\infty k^3\,\mathrm{d}k\int_{-1}^{1}\frac{s^2\mathrm{d}s}{(1-s^2)^{1/2}}\{e(k,s,0)-\mathrm{Re}[Z(k,s,0)\exp(\mathrm{i}4\Omega st)]\}. \quad (A\,2)$$

Hence, $L^2(\omega_1)$ tends to a constant for large Ωt, after a certain transient period.

https://doi.org/10.1017/jfm.2011.74 Published online by Cambridge University Press

	N	ℓ^B	$10^4\nu$	f_{min}	f_{min}	k_p	R_λ	R_L	$\langle\epsilon\rangle$	$10^3\eta$	L
Run I1	256	2π	15.0	6.5	9.5	8.0	48.0	93.2	0.482	9.15	0.242
Run I2	256	2π	20.0	9.5	12.5	11.0	33.5	56.6	0.740	10.2	0.196
Run I3	512	4π	15.0	6.5	9.5	8.0	48.4	93.5	0.475	9.18	0.243

TABLE 3. DNS parameters and characteristics of homogeneous isotropic turbulence at $t = 8$. The Kolmogorov length scale η is defined by $\eta = (\nu^3/\langle\epsilon\rangle)^{1/4}$. $k_{max} = 121$.

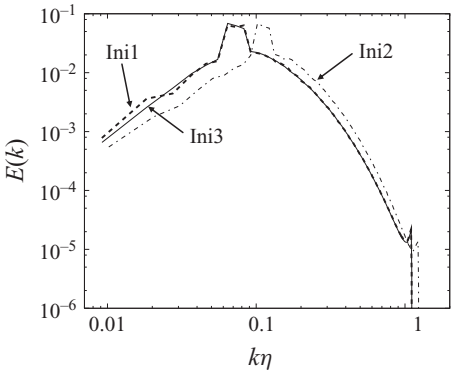


FIGURE 14. The energy spectra $E(k)$ at $t = 8$ in Ini1, Ini2 and Ini3.

A.2. *Initially homogeneous and isotropic turbulence*

Noting that $Z(\boldsymbol{k}, 0) = 0$ and equation (2.11) for initially homogeneous and isotropic turbulence, we find that both $L^2(\omega_1)$ and $L^3(\omega_1)$ must be time-independent in initial isotropic turbulence within the inviscid linear dynamics.

Appendix B. Initial velocity fields in the DNS of homogeneous rotating turbulence

In order to generate almost homogeneous isotropic initial conditions Ini1 and Ini2 in table 1 and Ini3 used in § 6.2, we performed a series of runs, say Runs I1, I2 and I3, respectively, by using an alias-free spectral method and a fourth-order Runge–Kutta method as used by the DNS in § 4.

Starting with an initial condition given by a random solenoidal velocity field with the energy spectrum $E(k) \propto k^4 \exp(-2k^2/k_p^2)$, we continued each run up to $t = 8$ where the energy dissipation rate $\langle\epsilon\rangle$ is statistically quasi-stationary (figure omitted). During the run, the total energy was kept almost time-independent and about 0.5 by introducing negative viscosity in the wavenumber range $f_{min} < k < f_{max}$.

The time increment is $\Delta t = 2.0 \times 10^{-3}$ in all the runs. Table 3 shows run parameters and the characteristic of the fields at $t = 8$, which corresponds to $14.6T$, $20.2T$ and $14.6T$, in Ini1, Ini2 and Ini3, respectively, in which T is initial large eddy turnover time defined by $T = L/u'$. We use the fields at $t = 8$ thus obtained as the initial fields Ini1, Ini2 and Ini3.

Figure 14 plots the energy spectra $E(k)$. The spectra sufficiently decrease as the wavenumber increases. The integral length scales in Ini1, Ini2 and Ini3 are sufficiently small compared to the side length of the periodic box, i.e. ℓ^B. The Taylor micro-scale Reynolds numbers R_λ in Ini1 and Ini2 are smaller than R_λ (100–160) so far reported

https://doi.org/10.1017/jfm.2011.74 Published online by Cambridge University Press

in DNS of homogeneous isotropic turbulence in a periodic box of size 2π which were performed with 256^3 grid points by the use of forcing at a lower wavenumber (see e.g. Jiménez *et al.* 1993; Kaneda *et al.* 2003).

REFERENCES

Bartello, P., Métais, O. & Lesieur, M. 1994 Coherent structures in rotating three-dimensional turbulence. *J. Fluid Mech.* **273**, 1–29.

Bellet, F., Godeferd, F. S., Scott, J. F. & Cambon, C. 2006 Wave turbulence in rapidly rotating flows. *J. Fluid Mech.* **562**, 83–121.

van Bokhoven, L. J. A., Cambon, C., Liechtenstein, L., Godeferd, F. S. & Clercx, H. J. H. 2008 Refined vorticity statistics of decaying rotating three-dimensional turbulence. *J. Turbul.* **9** (6), 1–24.

Bourouiba, L. & Bartello, P. 2007 The intermediate Rossby number range and two-dimensional–three-dimensional transfers in rotating decaying homogeneous turbulence. *J. Fluid Mech.* **587**, 139–161.

Cambon, C., Benoit, J. P., Shao, L. & Jacquin, L. 1994 Stability analysis and large-eddy simulation of rotating turbulence with organized eddies. *J. Fluid Mech.* **278**, 175–200.

Cambon, C. & Jacquin, L. 1989 Spectral approach to non-isotropic turbulence subjected to rotation. *J. Fluid Mech.* **202**, 295–317.

Cambon, C., Mansour, N. N. & Godeferd, F. S. 1997 Energy transfer in rotating turbulence. *J. Fluid Mech.* **337**, 303–332.

Cambon, C., Rubinstein, R. & Godeferd, F. S. 2004 Advances in wave turbulence: rapidly rotating flows. *New J. Phys.* **6**, 73.

Cambon, C. & Scott, J. F. 1999 Linear and nonlinear models of anisotropic turbulence. *Annu. Rev. Fluid Mech.* **31**, 1–53.

Chen, Q., Chen, S., Eyink, G. L. & Holm, D. D. 2005 Resonant interactions in rotating homogeneous three-dimensional turbulence. *J. Fluid Mech.* **542**, 139–164.

Craya, A. 1958 Contribution à l'analyse de la turbulence associée à des vitesses moyennes. *P. S. T. Ministère de l'Air,* p. 345.

Davidson, P. A., Staplehurst, P. J. & Dalziel, S. B. 2006 On the evolution of eddies in a rapidly rotating system. *J. Fluid Mech.* **557**, 135–144.

Galtier, S. 2003 Weak inertial-wave turbulence theory. *Phys. Rev.* E **68**, 015301(R).

Gence, J.-N. & Frick, C. 2001 Naissance des corrélations triples de vorticité dans une turbulence statistiquement homogène soumise à une rotation. *C. R. Acad. Sci. Paris* II B **329**, 351–356.

Herring, J. R. 1974 Approach of axisymmetric turbulence to isotropy. *Phys. Fluids* **17**, 859–872.

Hopfinger, E. J., Browand, F. K. & Gagne, Y. 1982 Turbulence and waves in a rotating tank. *J. Fluid Mech.* **125**, 505–534.

Hossain, M. 1994 Reduction in the dimensionality of turbulence due to a strong rotation. *Phys. Fluids* **6**, 1077–1080.

Jacquin, L., Leuchter, O., Cambon, C. & Mathieu, J. 1990 Homogeneous turbulence in the presence of rotation. *J. Fluid Mech.* **220**, 1–52.

Jiménez, J., Wray, A. A., Saffman, P. G. & Rogallo, R. S. 1993 The structure of intense vorticity in isotropic turbulence. *J. Fluid Mech.* **255**, 65–90.

Kaneda, Y., Ishihara, T., Yokokawa, M., Itakura, K. & Uno, A. 2003 Energy dissipation rate and energy spectrum in high resolution direct numerical simulations of turbulence in a periodic box. *Phys. Fluids* **15**, L21–L24.

Kolvin, I., Cohen, K., Vardi, Y., & Sharon, E. 2009 Energy transfer by inertial waves during the buildup of turbulence in a rotating system. *Phys. Rev. Lett.* **102**, 014503.

Liechtenstein, L., Godeferd, F. S. & Cambon, C. 2005 Nonlinear formation of structures in rotating stratified turbulence. *J. Turbul.* **6** (24), 1–18.

Moisy, F., Morize, C., Rabaud, M. & Sommeria, J. 2011 Decay laws, anisotropy and cyclone-anticyclone asymmetry in decaying rotating turbulence. *J. Fluid Mech.* **666**, 5–35.

Morinishi, Y., Nakabayashi, K. & Ren, S. Q. 2001 Dynamics of anisotropy on decaying homogeneous turbulence subjected to system rotation. *Phys. Fluids* **13**, 2912–2922.

https://doi.org/10.1017/jfm.2011.74 Published online by Cambridge University Press

Morize, C., Moisy, F. & Rabaud, M. 2005 Decaying grid-generated turbulence in a rotating tank. *Phys. Fluids* **17**, 095105.

Sagaut, P. & Cambon, C. 2008 *Homogeneous Turbulence Dynamics*. Cambridge University Press.

Smith, L. M. & Lee, Y. 2005 On near resonances and symmetry breaking in forced rotating flows at moderate Rossby number. *J. Fluid Mech.* **535**, 111–142.

Smith, L. M. & Waleffe, F. 1999 Transfer of energy to two-dimensional large scales in forced, rotating three-dimensional turbulence. *Phys. Fluids* **11**, 1608–1622.

Squires, K. D., Chasnov, J. R., Mansour, N. N., & Cambon, C. 1994 The asymptotic state of rotating homogeneous turbulence at high Reynolds numbers. In *Application of Direct and Large Eddy Simulation to Transition and Turbulence, Chania, Crete Greece*.

Staplehurst, P. J., Davidson, P. A. & Dalziel, S. B. 2008 Structure formation in homogeneous freely decaying rotating turbulence. *J. Fluid Mech.* **598**, 81–105.

Waleffe, F. 1992 The nature of triad interactions in homogeneous turbulence. *Phys. Fluids* A **4**, 350–363.

Waleffe, F. 1993 Inertial transfers in the helical decomposition. *Phys. Fluids* A **5**, 677–685.

Yeung, P. K. & Zhou, Y. 1998 Numerical study of rotating turbulence with external forcing. *Phys. Fluids* **10**, 2895–2909.

https://doi.org/10.1017/jfm.2011.74 Published online by Cambridge University Press